FIN UNSTEADY SURFACE PRESSURE EVALUATION DUE TO BUFFETING BASED ON MEASURED FLUCTUATING VELOCITIES

Dipl.-Ing. Christian Breitsamter
o. Prof. Dr.-Ing. Boris Laschka
Lehrstuhl für Fluidmechanik, Technische Universität München
Arcisstr. 21, D-80290 München, Germany

Abstract

A method to predict fin buffet aerodynamic loads using only flowfield characteristics, namely fluctuating velocity, is developed. The model tested is a high performance single–finned delta–canard configuration. Time–dependent velocities are measured in the fin region resulting in a detailed description of the properties of the buffeting–inducing flowfield associated with the bursting of the leading–edge vortices. In order to determine the unsteady fin surface pressure a modified lifting surface method is used. The input consists of fluctuating local incidence at a given set of collocation points calculated from the measured velocities. For a large number of discrete frequencies the amplitude value is derived from the incidence spectra. The prediction method provides root–mean–square and power spectral density distributions of fluctuating surface pressure as well as of fluctuating normal force. It is shown that unsteady surface pressure increases significantly with increasing angle of attack. The power spectral density of the buffet loads exhibit a strong narrow–band peak. It is related to quasi–periodic fluctuations present in the flow of the wing/canard vortex sheets approaching the midsection. The results obtained agree very well with direct measurements of the fin unsteady surface pressure. This gives strong evidence that fin buffet loads can be determined with adequate accuracy by that approach.

Nomenclature

Symbols:

A_j	finite Fourier transform at f_j
A_q, B_q	coefficients of finite Fourier series
c_N	normal force coefficient
c_r	wing root chord
$c_{p_{rms}}$	rms value of pressure coefficient
f	frequency, Hz
f_M	sampling frequency, Hz
f_N	Nyquist frequency, Hz
f_T	low–pass filter frequency, Hz
h	distance of sampled values, $1/f_M$
I_1	mod. Bessel function of 2nd kind, 1st order
K	Kernel function of lifting surface method
K_1	mod. Bessel function of 1st kind, 1st order
k	reduced frequency, fl_μ/U_∞
k'	reduced frequency, $fc_r \sin\alpha/U_\infty$
k_s	lifting surface red. frequency, $2\pi f s_F/U_\infty$
L_1	modified Struve function of 1st order
l_μ	wing mean aerodynamic chord
Ma_∞	freestream Mach number
N	number of sampled values
n_f	number of frequency intervalls
p	surface pressure
q_∞	freestream dynamic pressure
Re	Reynolds number, $U_\infty l_\mu/\nu$
S_{c_N}	power spectral density of c_N
$S_{v'}$	power spectral density of v'
$S_{\alpha'_F}$	power spectral densities of α'_F
$S_{\Delta c_p}$	power spectral density of Δc_p
s	wing half span
s_F	fin span
T	sampling time, sec
U_∞	freestream velocity
u, v, w	streamwise, lateral and vertical velocity components (wind tunnel-axis system)
u', v', w'	fluctuation part of u, v, w
v_{rms}	rms lateral velocity, $\sqrt{\overline{v'^2}}$
X, Y	fin nondimensionalized coordinates, referred to local chord and fin span
x, y, z	streamwise, lateral and vertical coordinates of the wind tunnel–axis system; lifting surface coordinates
x_F, z_F	fin coordinates
α	aircraft angle of attack
α_F	fin local incidence
$\overline{\alpha}_F$	mean value of α_F
α'_F	fluctuating part of α_F
$\hat{\alpha}$	amplitude of harmonically fluct. incidence
β	aircraft angle of sideslip
β^2	Prandtl factor, $1 - Ma_\infty^2$
Δc_p	coefficient of pressure difference between both sides of the lifting surface, $\Delta p/q_\infty$
$\Delta c_{p_{rms}}$	rms value of Δc_p
φ_W	wing leading–edge sweep
φ_C	canard leading–edge sweep
φ_F	fin leading–edge sweep
Λ, Λ_F	wing aspect ratio, fin aspect ratio
λ, λ_F	wing taper ratio, fin taper ratio
ν	kinematic viscosity
ω	angular frequency

Abbreviations:

rms	root-mean-square

Introduction

For the generation of modern fighter aircraft fitted with slender wing geometry and canard as well as conventional aft control surfaces the capability of supermaneuvering has been well demonstrated. It is associated with controlled

flight at α near or exceeding maximum lift. However, in the high-α flight regime the aircraft experience severe fin buffeting which is attributed to the highly turbulent flow caused by bursted leading-edge vortices.[1-4] The induced narrow-band aerodynamic loads may excite at the natural frequencies the fin structure. They constitute a threat to the fin structural integrity and corrective actions may be required to ensure both vibration-free control and long fatigue life.[5,6]

In particular, at twin-tailed fighter aircraft (F/A-18, F-15) the fin buffeting problem became a crucial issue. Comprehensive investigations have been conducted aimed at understanding and reducing the buffeting loads.[7-13] The majority of data is related to small-scale wind tunnel tests. The data base is complemented by results of some full-scale model tests[14] and flight test data.[15] The single-finned X-29 and X-31 research vehicles were also affected by fin buffeting.[16] Furtheron, data on buffet loads were obtained from small-scale tests on a high-speed slender-wing transport aircraft.[17]

An extensive investigation on the fin flow environment of a delta-wing model with canard stabilizer and a single center-line fin was started at the Lehrstuhl für Fluidmechanik of the Technische Universität München. The turbulent flow structure in the fin region was well defined by the spatial and temporal characteristics of the time-dependent flow velocities resulting in a general treatment of the fin buffeting problem. Reference 1 shows results at symmetric freestream. The flow properties at sideslip are reported in Ref. 2. The behaviour of the flow quantities is shown to be significant for the vortex breakdown flowfield. An annular structure assigned to the remaining swirling vortex sheet is the locus of maximum turbulence intensity. There, the fluctuations are channeled into a narrow-band arising from a helical mode instability. This was proved studying both unsteady flowfield velocity and associated surface pressure fluctuations on a slender delta wing when fully developed as well as bursted leading-edge vortices are present.[18] For the development and validation of computational prediction methods the detailed flowfield surveys are of distinct utility.

Within a numerical treatment of the buffeting problem the features of the very complex vortical flowfield must be simulated correctly. The methods used are typically based on the Reynolds-averaged Navier-Stokes equations related to finite difference techniques. Dealing with complete aircraft configurations the flow calculation requires a tremendous amount of computational time and storage capacity. The Reynolds number has a strong bearing on the run-times, because higher Reynolds number mean thinner shear layers and denser grids. The methods are quite succesful when simulating the pre-burst vortex structure and burst locations even for complex geometries,[19-21] but quantitative details within the burst region have proved elusive. In Reference 22 the computational demands for wholly theoretical response predictions are quantified. The conclusion was drawn that the computational time must decrease three orders of magnitude to bring such predictions down to feasible size.

All response analysis to date have relied on experimental data for the pressure inputs.[5,23,24] The stress analysis and fatigue estimates use data of fin aerodynamic loads obtained by direct steady and unsteady pressure measurements at sufficient points on the fin surface. Most of the experiments were conducted on rigid wind-tunnel models employing the results for the full-scale aircraft design.

In general, Reynolds number and Mach number matching is required to extrapolate small-scale data to flight conditions. Because of leading-edge flow separation and high turbulence intensity within the breakdown flowfield the influence of Reynolds number is rather small. At the α of interest, maneuvering aircraft would experience large normal loads, how most flight is limited to lower Mach numbers.[5] Thus, compressibility effects, although present, are not of primary issue. In this context it was shown that buffet spectra could be extrapolated over large ranges of velocity, and model size, and that they could be used to predict flight loads.[23]

Present Scope and Objectives

The present investigation focus on the prediction of fin buffet aerodynamic loads. The buffeting excitation input is well defined by the lateral turbulence intensity and related power spectral density distributions. A modified lifting surface method is used to evaluate unsteady fin surface pressure. Hence, the predicition method is based only on features of the flowfield which are dependent on the aircraft configuration and aerodynamic conditions such as Mach number, angle of attack and angle of sideslip. As any aircraft model can be used this results in a significant reduction of model costs. It leads also to a downgrade of priority for expensive fin models instrumented with a large number of pressure transducers. Those models have to be constructed in a preliminary design stage and cannot be adapted, in general, to design modifications. Only limited high-speed wind tunnel data and some flight data are necessary to be used as check points, to predict the fin-buffeting full-scale flight environment.

Measurement Technique and Test Program

Description of Model and Facility

The wind-tunnel model used represents a high-agility aircraft of canard-delta wing type. The geometry is shown in Fig. 1. Major parts of the model are: nose section; front fuselage including rotatable canards and a single place canopy; center fuselage with delta-wing section and a through-flow double air intake underneath; and rear fuselage including nozzle section. All pieces are made of stainless steel. They are designed with close tolerance fits and are doweled and screwed together. The single fin is part of a steel insert that is bolted to the rear fuselage. Leading- and trailing-edge flaps are fastened to the wings by lap elements. Their bolt pins assure accurate adjustment. The canard setting angle may be changed via integral shafts that are linked to a self-locking computer controlled gear mechanism installed in a cavity under the canopy. Within the tests, the leading- and trailing edge flap deflections as well as the canard setting angle were set at 0 deg. Engine ducts and flow passages were not blocked.

$2s = 0.740$ m	$\varphi_W = 50°$
$l_\mu = 0.360$ m	$\varphi_C = 45°$
$\Lambda = 2.45$	$\lambda = 0.14$

$s_F = 0.47\ s$	$\varphi_F = 54°$
$\Lambda_F = 1.38$	$\lambda_F = 0.19$

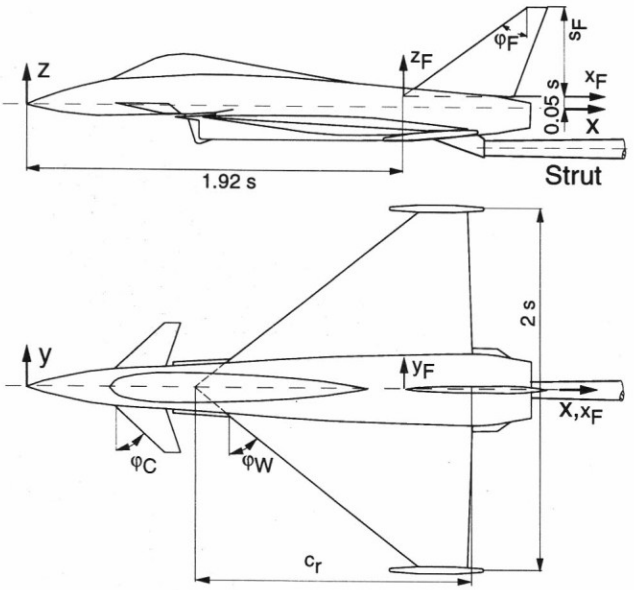

Fig. 1 Geometry of delta–canard model.

The model was sting mounted on its lower surface from a moving support strut (Fig. 2). This arrangement enables flowfield measurements to a great extent free from interference. The computer controlled model support provides an incidence range from 0 to 31.5 deg and models may be yawed and rolled 360 deg.

$U_\infty \longrightarrow$

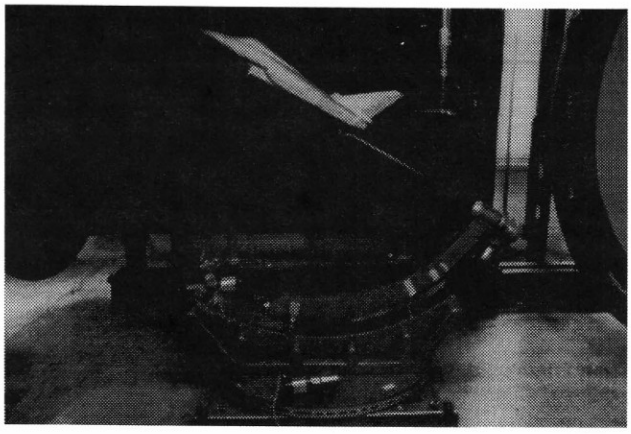

Fig. 2 Model mounted in the test section.

Nozzle diam.	1.50 m
Length of test section	3.00 m
Maximum power	85 kW
Maximum usable velocity	55 m/s
Turbulence intensity	0.3% – 0.4%

Table 1 Operational data of wind tunnel facility.

The experiments were conducted in a low–speed wind tunnel facility of the Lehrstuhl für Fluidmechanik of the Technische Universität München. The wind tunnel is of the Göttingen type, the test section is open. Operational data are collected in Table 1.

The wind tunnel data acquisition and control system is based on a personal computer with a high–speed board (DT 2821-F16-SE). This enables automated data sampling of hot–wire, pressure and temperature signals as well as the control of the wind tunnel, the 3–axis probe–traversing system and the 3–axis model support. Wind tunnel reference data are taken to ensure that the experiment is progressing properly. Data acquisition software has been developed which allows fully automated surveys of flowfields around models of arbitrary geometrical shape. A local network provides online data transfer and communication with host computers, namely a CONVEX C1 and a CRAY Y-MP, which are required for data reduction and processing by statistical means.

Measurement of time–dependent velocity

Dual–sensor hot–wire probes (DISA 55P61) were used to measure the fluctuating velocity components. The sensors consist of 5–μm–diam. platinum–plated tungsten wires giving a length/diam. ratio of 250. The wires form a measuring volume of approximately 0.8 mm in diam. and 0.5 mm in height. A sensor angle of 45 deg was chosen assuming that the best angular resolution will be obtained with pairs of perpendicular wires.

The probes were operated by a multi–channel constant–temperature anemometer system (DISA C). By means of its signal conditioner modules, bridge output voltages were low–pass filtered at 1000 Hz before digitization and amplified for optimal signal level. The signals were then digitized with 12–bit precision through the sixteen–channel simultaneous–sampling A/D converter installed on the PC high–speed board. The sampling rate f_M for each channel was set to 3000 Hz giving a Nyquist frequency f_N of 1500 Hz. The sampling time T is 38.4 sec. Thus each sample block N contains 115200 points in the time domain, producing 57600 points in the complex frequency domain. The sampling parameters were arrived at by preliminary tests to ensure that all significant flowfield phenomena are detected. Statistical accuracy of the calculated quantities was considered as well. The sampling parameters are related to an statistical error of 0.2, 1 and 3% for the mean and standard deviation and spectral density estimation, respectively.

The use of a cross–wire configuration generally assumes some knowledge of the flowfield, such as a known flow direction to which the probe must be aligned. The nature of the vortex–dominated flow precludes any knowledge on the direction of the velocity vector everywhere in the field, save for the axial component which is assumed to be always in the positive x–direction. In order to determine all three velocity components (u, v, w) the probe has to be rotated around its axis by 90 deg to adjust the wire plane once horizontal and once vertical against the main flow direction (quadrupel–probe). Thus, two triggered traverse sweeps are necessary to obtain the streamwise (u), lateral (v) and vertical (w) components, respectively. Each digitized and tem-

perature corrected voltage-pair of the corresponding probe positions was converted to evaluate the time-dependent velocity vector. The numerical method used is based on look-up tables derived from the full velocity- and flow angle calibration of the sensors. A detailed description is given in Refs. 25 and 26.

Description of Tests

Flowfield measurements were performed at discrete points in the fin region, corresponding to lifting surface collocation points (Fig. 3). The fin section was removed to encounter only the flowfield input. The tests were made at five angles of attack, namely 20, 25, 28, 30, and 31.5 deg, and at sideslip $\beta = 0$, and 5 deg. The freestream reference velocity U_∞ was hold constant at 40 m/s corresponding to $Ma_\infty = 0.12$. This gives a Reynolds number of $Re = 0.97 \times 10^6$ based on the wing mean aerodynamic chord for all the results presented. Further test section conditions were ambient static pressure and temperature. At all tests turbulent boundary layers were present at wing and control surfaces proved by shear-stress sensitive liquid crystal measurements.[27]

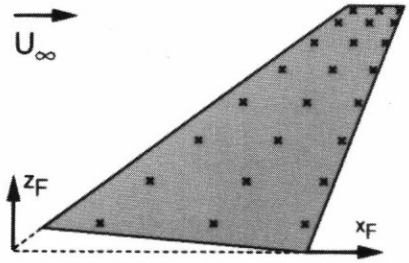

a) 3×8 points

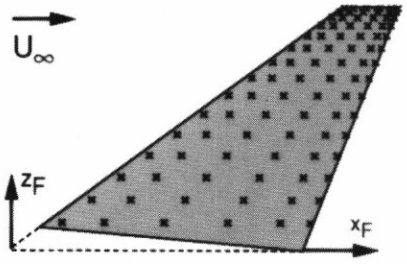

b) 6×15 points

Fig. 3 Measurement stations in the fin region and fin collocation points, respectively.

Buffeting-Inducing Flowfield

In order to quantify the buffeting excitation level the flowfield is carefully described by the velocity fluctuations. They are related to random ergodic (stationary) timeseries. For a single fin mainly the lateral velocity causes buffeting, whereas for a twin-fin with dihedral, both the lateral and the vertical velocity contribute.[1]

Lateral Turbulence Intensity Distributions

The rms values of fluctuating velocity v_{rms} provide a measure of the intensity of the fluctuating input. They are typically nondimensionalized by the freestream velocity U_∞ to present the relative turbulence intensity in terms of percent of freestream.

A-A Vortex structures in a plane normal to the fin surface at $x_F/s = 0.54$ (95% fin root chord), view from behind; Ref. 1
WLV Wing leading-edge vortex
CLV Canard leading-edge vortex
CTV Canard trailing-edge vortex

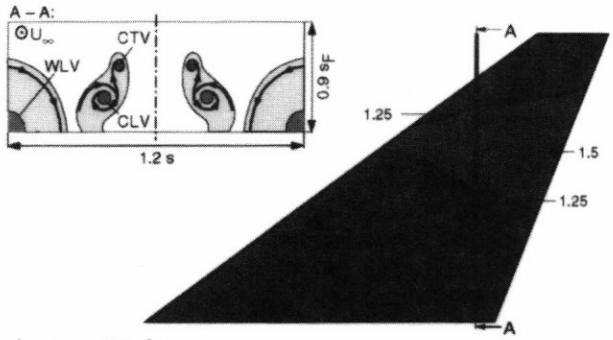

a) $\alpha = 20$ deg

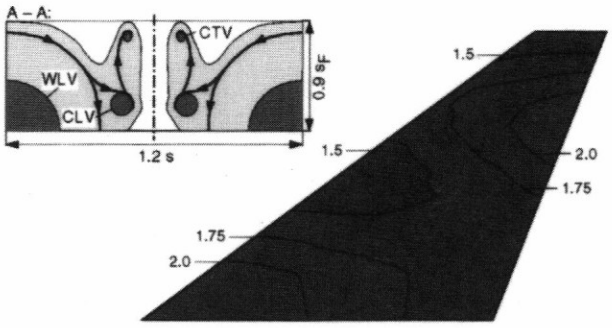

b) $\alpha = 25$ deg

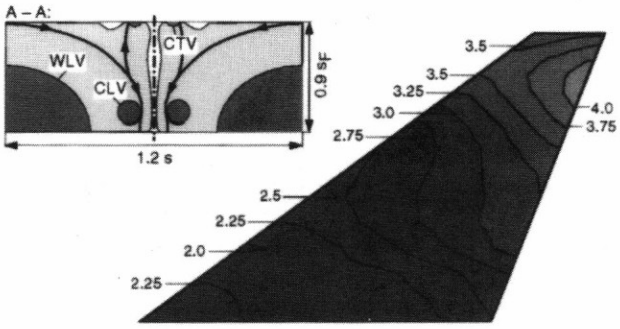

c) $\alpha = 30$ deg

Fig. 4 rms velocity contours v_{rms}/U_∞ at $\alpha = 20$, 25, and 30 deg and $\beta = 0$ deg; (Values in percent).

Figure 4 depicts rms velocity contours for symmetric flow conditions at $\alpha = 20$, 25, and 30 deg. The rms velocity fluctuations at $\alpha = 20$ deg are relatively low. They are characterized by a homogeneous distribution over the whole fin section (Fig. 4a). At this α the fin flow environment is only little affected by the wing or canard vortex systems. With increasing incidence the bursted wing leading-edge vortices expand and move inboard and upwards. Through wing influence the canard vortex system is shifted inwards and downwards. Thus, the canard leading-edge vortices merge completely with the inboard part of the wing leading-edge vortex sheets while the canard trailing-edge vortices are detached upwards.[1] Because of this, the fin flowfield takes on a dramatically different character at $\alpha = 25$ deg, which is evident by considerably increased rms values (Fig. 4b).

A–A Vortex structures in a plane normal to the fin surface at $x_F/s = 0.54$ (95% fin root chord), view from behind; Ref. 2
WLV Wing leading-edge vortex
CLV Canard leading-edge vortex
CTV Canard trailing-edge vortex
CAV Canopy vortex system

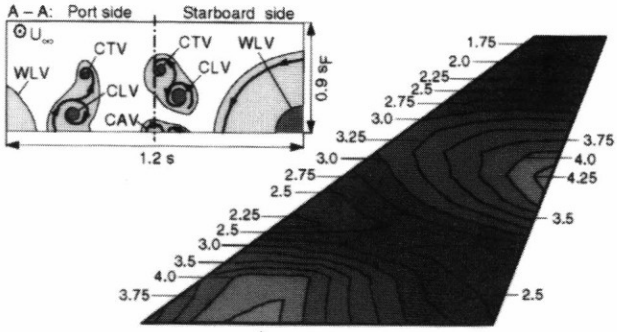

a) α = 20 deg

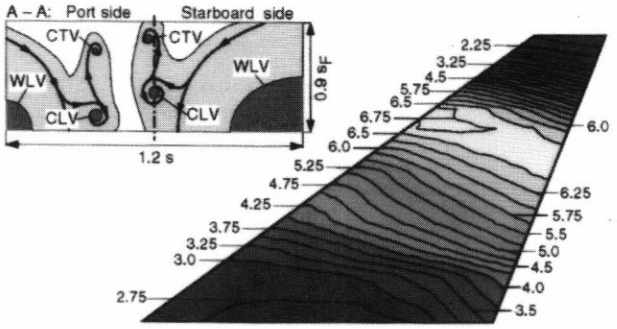

b) α = 25 deg

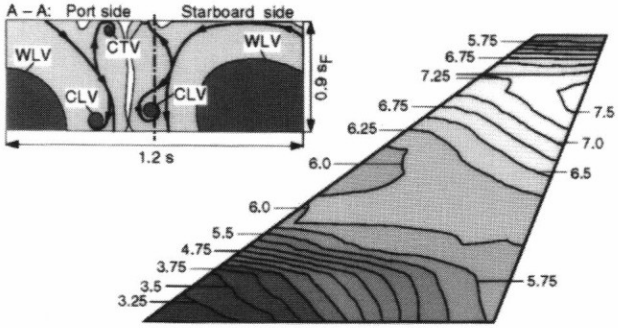

c) α = 30 deg

Fig. 5 rms velocity contours v_{rms}/U_∞ at α = 20, 25, and 30 deg and β = 5 deg; (Values in percent).

Maximum values in v_{rms} are found at the root of the fin close to its leading-edge and at 65% span close to its trailing-edge. The first arises from the canard leading-edge vortices, the second from the canard trailing-edge vortices. At α = 30 deg, the process of vortex interaction described above continues. It results in maximum rms values near the tip of the fin (Fig. 4c).

At sideslip β = 5 deg, the starboard wing and canard vortex systems are shifted inboard dominating the flow behaviour in the midsection.[2] Contours of v_{rms} are shown in Fig. 5. At α = 20 deg, the rms values have increased to three times the level of symmetric flow conditions (Fig. 5a). A vortex pair shed at the canopy evoke a rms maximum at the root of the fin. A second rms maximum located near the mid-

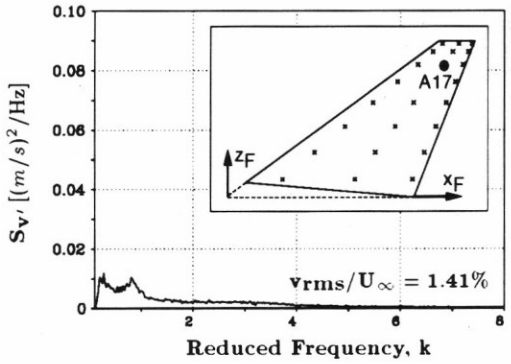

a) α = 25.0 deg, β = 0 deg

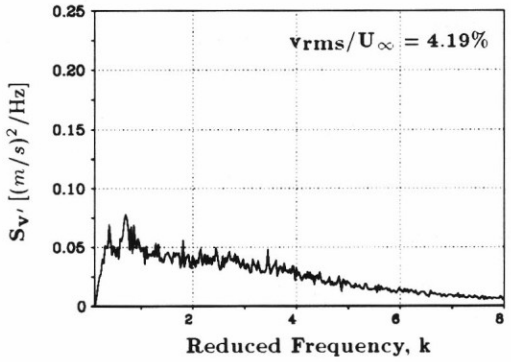

b) α = 25.0 deg, β = 5 deg

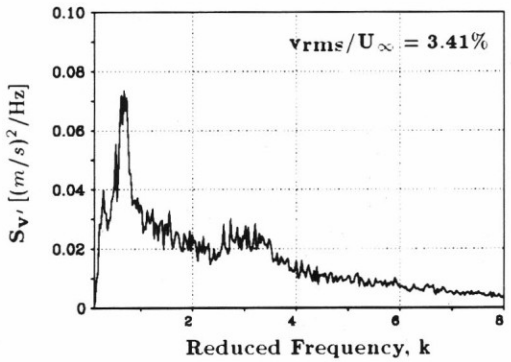

c) α = 30.0 deg, β = 0 deg

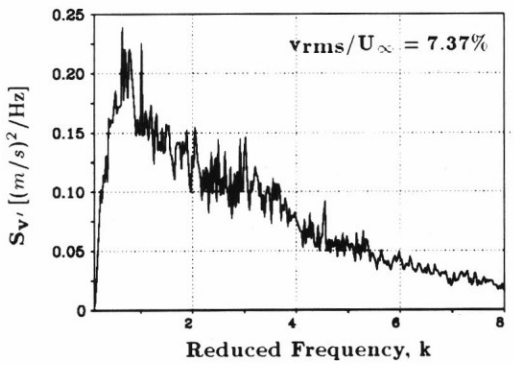

d) α = 30.0 deg, β = 5 deg

Fig. 6 Spectra of fluctuating lateral velocity v' at station A17 (X = 0.611, Y = 0.831) at α = 25, and 30 deg and β = 0, and 5 deg.

span close to the trailing–edge is caused by the canard vortex system. The pattern in lateral turbulence intensity is shown to be very different at $\alpha = 25$ deg, where the rms values are the largest in a region at 60% span covering a small area from the leading– to the trailing–edge (Fig. 5b). Values of v_{rms} decreas towards the root and the tip of the fin. The region of maximum rms values is related to the starboard wing leading–edge vortex sheet approaching the midsection, in particular, to that part where the canard leading–edge vortex is embedded. At $\alpha = 30$ deg, the region of maximum lateral turbulence intensity has grown both in size and strength (Fig. 5c). It is placed closer to the fin tip due to the starboard wing leading–edge vortex which moves upwards and becomes enlarged.

Character of the Spectral Content

Velocity spectra are shown in Fig. 6 for $\alpha = 25$, and 30 deg and $\beta = 0$, and 5 deg at station A17 ($X = 0.611, Y = 0.831$). The power spectral density is evaluated with 512 band–averaged and hanning–windowed frequency intervals. For the Nyquist frequency of 1500 Hz as given above, the frequency resolution is 2.93 Hz corresponding to a Δk of 0.026.

After the rapid expansion of the vortex core due to burst the flow changes to a highly turbulent swirling state where large narrow–band velocity fluctuations occur.[1,2] In the midsection, a narrow–band concentration of kinetic turbulent energy is detected the first time at $\alpha = 25$ deg (Figs. 6a and 6b). As substantiated in Ref. 1, the distinct frequency peak centered around $k = 0.9$ coincides with the sharp peaks detected in the shear layer velocity spectra of the bursted wing leading–edge vortices. In Reference 18 it is pointed out that the vortex breakdown flow is subject to a helical mode instability producing quasi–periodic velocity fluctuations that in turn gives rise to coherent pressure fluctuations. At $\alpha = 30$ deg, the fin flow encounters more extensively the vortex breakdown flow resulting in pronounced frequency peaks of $k = 0.6 - 0.8$ (Fig. 6c). The spectra depict a second frequency hump around $k = 3.0$ which refers to the canard vortex system. During the merging process of wing and canard vortex sheets both vortex burst frequencies are present. At sideslip, the fin flow comes in strong contact with the vortex core flow, how the spectra becomes widened and the overall level of turbulent kinetic energy increases (Fig. 6d).

Evaluation of Buffeting–Induced Fin Surface Pressure

As shown in the previous section the statistical properties of the buffeting–inducing turbulent flowfield are well known. Therefore, classical unsteady aerodynamic theory might be suitable for predicting the pressures and airloads produced thereby. In the present study a modified lifting surface method is applied which is based on unsteady subsonic potential flow. Fundamentals are given by B. Laschka.[28]

Integral Equation

The Küssner integral equation reflects the relation between the angle–of–attack and pressure distributions of harmonically oscillating lifting surfaces.

$$\alpha(x,y) = \frac{1}{8\pi}\int_{-s}^{s}\int_{x_v(y')}^{x_h(y')} \Delta c_p(x',y') \times K(x,y;x',y')\,dx'\,dy' \qquad (1)$$

Related coordinates and dimensions are defined in Fig. 7. Eq. (1) can as well be used for a static surface (fin) in a flowfield, where the normalwash as function of x and y changes harmonically.

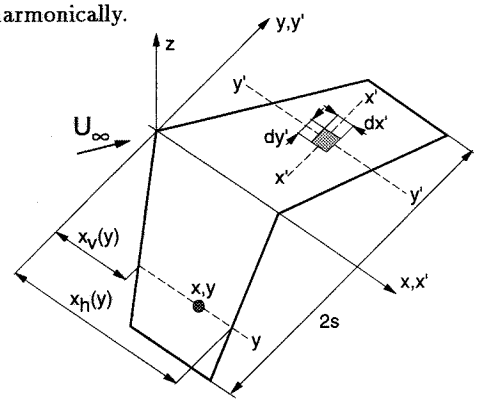

Fig. 7 Coordinates and dimensions of lifting surface method.

The unknown quantity is the pressure distribution Δc_p. It denotes the pressure difference between the both sides of the surface Δp referred to freestream dynamic pressure q_∞:

$$\frac{\Delta p(x,y)}{q_\infty} = \Delta c_p(x,y)\, e^{i\omega t} \qquad (2)$$

Due to harmonic motions the amplitude of the angle–of–attack distribution $\hat{\alpha}(x,y)$ yields:

$$\alpha(x,y,t) = \hat{\alpha}(x,y)\, e^{i\omega t} \qquad (3)$$

According to References 28 and 29, the Kernel function $K(x,y;x',y')$ was reduced into a form suitable for numerical and analytical solutions:

$$K(x,y;x',y') = \frac{e^{-ik_s(\xi-\xi')}}{s^2(\eta-\eta')^2}\left\{-k_s|\eta-\eta'| \left[K_1(k_s|\eta-\eta'|) + \frac{\pi i}{2}\Big(I_1(k_s|\eta-\eta'|) - L_1(k|\eta-\eta'|)\Big) - i - i\int_0^{UB}\frac{\tau}{\sqrt{1+\tau^2}}e^{ik_s|\eta-\eta'|\tau}d\tau\right] - \frac{\xi-\xi'}{\sqrt{(\xi-\xi')^2+\beta^2(\eta-\eta')^2}} e^{\frac{ik_s}{\beta^2}(\xi-\xi'-Ma_\infty\sqrt{(\xi-\xi')^2+\beta^2(\eta-\eta')^2}}\right\} \qquad (4)$$

$$\text{with} \quad UB = \frac{\xi-\xi'-Ma_\infty\sqrt{(\xi-\xi')^2+\beta^2(\eta-\eta')^2}}{|\eta-\eta'|\,\beta^2}$$

The dimensionless coordinates ξ, ξ', η, η' and the reduced frequency k_s are referred to the semi–span s. I_1 and K_1 are modified Bessel functions of first and of second kind and of first order; L_1 denotes a modified Struve function of first order.

The unknown pressure distribution $\Delta c_p(x, y)$ is approximated by means of adequate functions in chordwise and spanwise direction. After introducing those functions into the integral equation, Eq. (1), a system of linear equations results. The normalwash condition may be fullfilled in a number of collocation points (X, Y) which correspond to the number of functions. Modifications were made to consider high frequency input and an arbitrary number of collocation points in chord direction. The course of solution is described in detail in Ref. 30.

Buffeting Excitation Input

The local time–dependent incidences $\alpha'_F(X, Y)$ responsible for fin buffeting can be easily calculated from the measured fluctuating velocities acting in a plane perpendicular to the fin surface. This is shown in Fig. 8 with respect to a single center–line fin as well as to a twin–fin with dihedral.

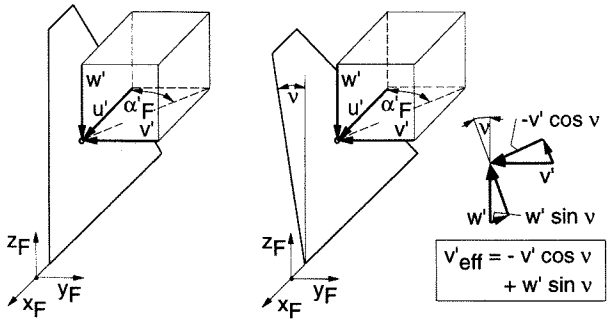

a) Center–line fin $\alpha'_F = \tan(v'/u')$ b) Fin with dihedral (ν) $\alpha'_F = \tan(v'_{eff}/u')$

Fig. 8 Local time–dependent fin incidence α'_F.

Due to the concept of small disturbances in linear potential theory one can infer that the magnitude of the fluctuating incidences are in the vicinity of 6 deg or less. This is substantiated by a representative plot of the α_F–timeseries (Fig. 9).

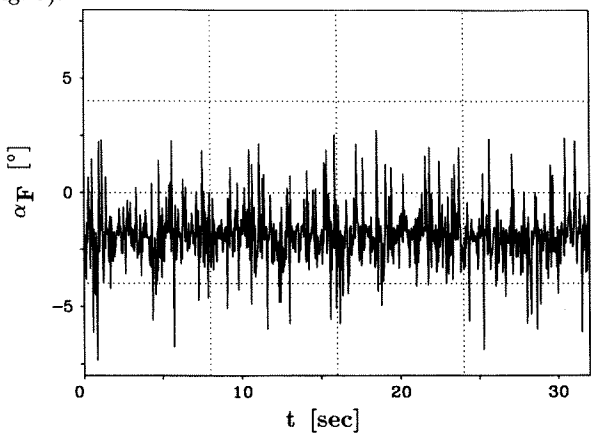

Fig. 9 Timeseries of fin local incidence at station A17 at α = 31.5 deg and β = 0 deg.

The mean incidence $\overline{\alpha}_F$ of the fin(s) at zero sideslip is known to be quite small. Regarded as a source of "interference" airloads the turbulence seems therefore unlikely to cause flow separation. For the tested center–line fin this is proved by lyquid crystal measurements.[27] However, the highly turbulent breakdown flowfield transfers its unsteadiness by induction effects to the attached flow on the fin. At sideslip or at twin–fin stations, the turbulence intensity becomes strongly increased. As documented in Ref. 31, the inboard and outboard surfaces of F/A–18 twin–fins at high–α enveloped by the wake of the bursted LEX–vortices show regions of highly unsteady and even totally separated flow.

Adopting the lifting surface method the local incidences $\alpha'_F(t)$ may be expressed as a series of superimposed harmonically oscillations derived from fourier analysis of discrete values.[32] The sample record $\alpha'_F(t)$ (zero mean) is of finite length T, the fundamental period of the data. The record is sampled at an even number of N equally spaced points a distance h apart; $T = Nh$.

$$\alpha'_{F_n} = \alpha'_F(n\,h) \qquad n = 1, 2, \ldots, N \tag{5}$$

For a finite version of a Fourier series which will pass through these N data values holds:

$$\alpha'_{F_n} = \sum_{q=1}^{N/2} A_q \cos\left(\frac{2\pi q n}{N}\right) + \sum_{q=1}^{(N/2)-1} B_q \sin\left(\frac{2\pi q n}{N}\right) \tag{6}$$

$$A_q = \tfrac{2}{N} \sum_{n=1}^{N} \alpha'_{F_n} \cos\left(\tfrac{2\pi q n}{N}\right); \quad q = 1, 2, \ldots, \tfrac{N}{2} - 1$$

$$B_q = \tfrac{2}{N} \sum_{n=1}^{N} \alpha'_{F_n} \sin\left(\tfrac{2\pi q n}{N}\right); \quad q = 1, 2, \ldots, \tfrac{N}{2} - 1$$

A finite–range Fourier transform can be used to compute the coefficients A_q and B_q. The Fourier components A_j of the selected frequencies f_j are defined by

$$f_j = j/T \qquad j = 0, 1, \ldots, N-1$$

$$A_j = \frac{A(f_j,T)}{h} = \sum_{n=0}^{N-1} \alpha'_{F_n} e^{-i(2\pi j n/N)} \tag{7}$$

where h has been included with $A(f_j)$ to have a scale factor of unity before summation. Note that results are unique only out to $j = N/2$ since the Nyquist cutoff frequency f_N occurs at this point. The power spectral density $S_{\alpha'_F}(X, Y)$ and the cross spectral density between a reference point (X_R, Y_R) and the considered station (X, Y) $S_{\alpha'_F}(X_R, Y_R; X, Y)$ becomes

$$S_{\alpha'_F}(X, Y; f_j) = \frac{2\,h}{N} |A_j(X, Y)|^2 \tag{8}$$

$$S_{\alpha'_F}(X_R, Y_R; X, Y; f_j) = \frac{2\,h}{N} A_j^*(X_R, Y_R)\, A_j(X, Y) \tag{9}$$

where $A^*(f_j)$ is the complex conjugate of $A(f_j)$.

In order to reduce the amount of considered discrete frequencies the relevant frequency range of the incidence spectra $0 \le f \le f_T$ is divided into $n_f = 512$ intervals Δf. For

each centered discrete frequency

$$f_l = \frac{(2\,l+1)\,f_T}{2\,n_f} \qquad l = 0, 1, \ldots, n_f - 1$$

the amplitude $\hat{\alpha}'_F(f_l)$ is determined from the power spectral density $S'_{\alpha_F}(f_l)$

$$\hat{\alpha}'^2_F(f_l) = 2 \int_{f_l - \Delta f/2}^{f_l + \Delta f/2} S_{\alpha'_F}(f)\,df \qquad (10)$$

carried out at all collocation points (X, Y). This implies the conservative assumption of 100% spatial correlation. From further measurements with two hot-wire probes, one hold fixed at the reference point (X_R, Y_R), cross spectra of local incidence give information about phase shift.

Hence, the input quantities of the lifting surface code consist of reduced frequency k_{s_l}, the related amplitude of local incidence $\hat{\alpha}'_F(X, Y, k_{s_l})$, and freestream Mach number Ma_∞. The code provides the unsteady fin surface pressure distribution $\Delta c_p(X, Y, k_{s_l})$. From this, the power spectral density $S_{\Delta c_p}(X, Y)$ and the rms of the pressure fluctuations $\Delta c_{p_{rms}}(X, Y)$ are obtained. Integrating the unsteady pressure distribution the power spectral density of the normal force coefficient S_{c_N} is gained.

Results and Discussion

Intensity of Calculated Pressure Fluctuations

The rms values of the fluctuations in fin surface pressure difference $\Delta c_{p_{rms}}$ are shown in Figs. 10 and 11 refering to the conditions of Figs. 4 and 5. The pattern of the intensity of the unsteady pressure fluctuations corresponds to that of fluctuating lateral velocity. This is caused by the linear relationship between the amplitude functions of local incidence and pressure, Eq. (1). At $\alpha = 20$ deg and $\beta = 0$ deg the pressure fluctuations are very low as the bursted leading-edge vortices are less expanded and located outwards (Fig. 10a). At $\alpha = 25$ deg the inboard shift of the wing leading-edge and the canard vortices, both strongly connected by their shear layers, accounts for the two regions of maximum rms values (Fig. 10b). The pattern of $\Delta c_{p_{rms}}$ is significantly changed at $\alpha = 30$ deg (Fig. 10c). The fin encounters high pressure fluctuations increasing from the root to the tip where a maximum exists close to the trailing-edge. The source of this maximum is the unsteadiness produced by the inboard part of the wing leading-edge vortex sheet touching the midsection.

At $\beta = 5$ deg and $\alpha = 20$ deg, the behaviour in $\Delta c_{p_{rms}}$ is such that two regions of increased pressure fluctuations are present (Fig. 11a). One maximum is located at the root near the leading-edge. Upwards a local minimum at 16% span the rms values increase in span direction to form a second maximum at the midspan trailing-edge. Up to the fin tip a strong decrease in rms is observed. The pattern of $\Delta c_{p_{rms}}$ is completely different at $\alpha = 25$ deg (Fig 11b). There, the largest rms values are in a region above 50% span which covers the whole local chord. With increasing α this region is shifted upwards being extended at the same time. At $\alpha = 30$ deg, the peak values reach levels up to 32% (Fig. 11c). The type of behaviour in the pressure fluctuations can be subjected again to the development and interaction of the wing and canard vortex systems as it was shown within the flowfield discussion.

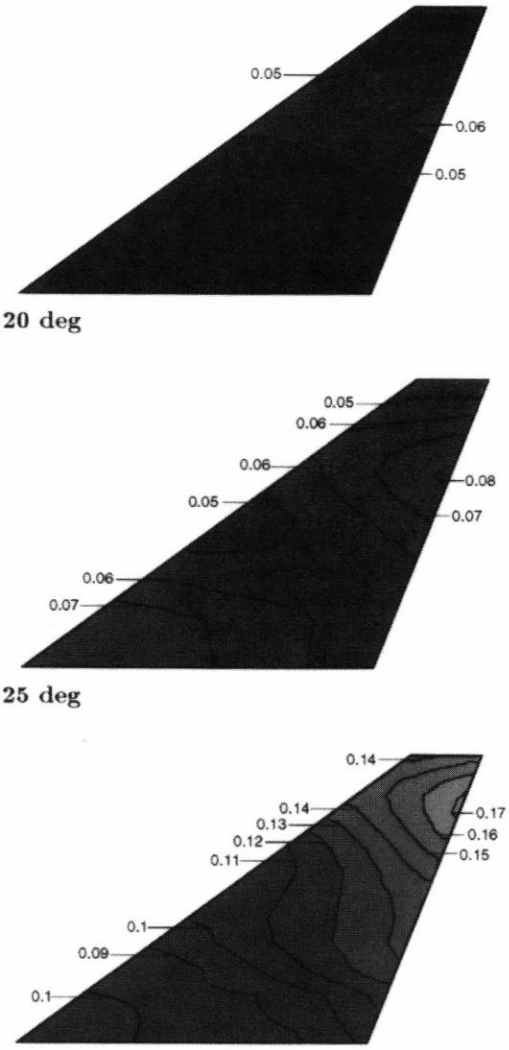

a) $\alpha = 20$ deg

b) $\alpha = 25$ deg

c) $\alpha = 30$ deg

Fig. 10 rms pressure contours $\Delta c_{p_{rms}}$ at $\alpha = 20$, 25, and 30 deg and $\beta = 0$ deg.

In order to verify the results of the lifting surface method the calculated pressure fluctuation intensity $c_{p_{rms}}$ is compared to that of unsteady pressure measurements.[30] The standard fin was replaced by an extensively instrumented fin, equipped with 24 Kulite XCQ-062-1.7 bar A absolute pressure transducers. Thereby, unsteady pressure signals were sampled at 12 positions directly opposite to each other on each surface. Test conditions refer to $Ma_\infty = 0.5$, $q_\infty = 14.9$ kPa and $Re = 3.0 \times 10^6$. Leading- and trailing-edge flap deflections were set to -20, and 20 deg, respectively, the canard setting angle was set to -10 deg. Pressure signals were amplified, band-pass filtered with low cutoff frequency of 5 Hz, high cutoff frequency of 1000 Hz, and digitized with a 12 bit ADC. The sampling rate for each channel was 6250 Hz providing 8000 samples within 1.28 sec.

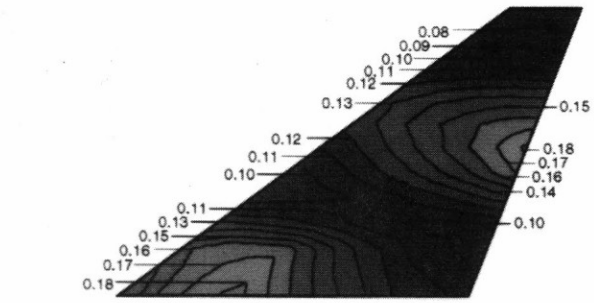

a) $\alpha = 20$ deg

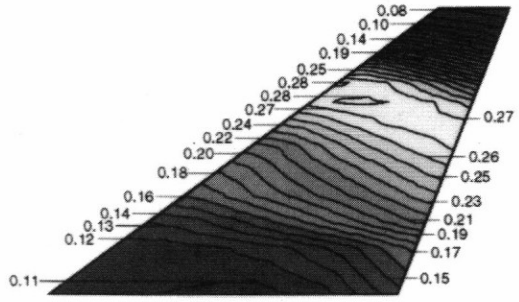

b) $\alpha = 25$ deg

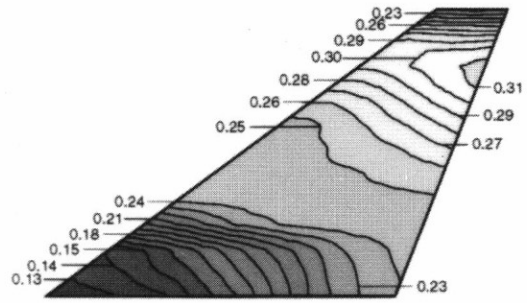

c) $\alpha = 30$ deg

Fig. 10 rms pressure contours $\Delta c_{p_{rms}}$ at $\alpha = 20$, 25, and 30 deg and $\beta = 5$ deg.

Within the lifting surface method values of $c_{p_{rms}}$ corresponding to one side of the surface are obtained by

$$c_{p_{rms}} = \frac{1}{2} \Delta c_{p_{rms}} \tag{11}$$

This is based on the conservative assumption that the amplitude functions of fluctuating pressure at stations opposite to each other act with the same mode. As depicted in Fig. 12, both measured and calculated $c_{p_{rms}}$ are averaged for one side and plotted together as a function of angle of attack. For the calculated $c_{p_{rms}}$ a vertical bar represents the scope of the respective minimum and maximum whereas the grey colored area reflects the range of minimum and maximum measured values. At symmetric freestream there is an excellent agreement between the measured and the calculated values of $c_{p_{rms}}$ (Fig. 12a). As concluded from the contour plots the magnitude of pressure fluctuations increases upwards $\alpha = 20$ deg where a significant rise starts at $\alpha = 25$ deg. The gradient in the $c_{p_{rms}}$ curve is well represented by the calculated values. At $\beta = 5$ deg, the values of $c_{p_{rms}}$ obtained with the lifting surface code corresponds

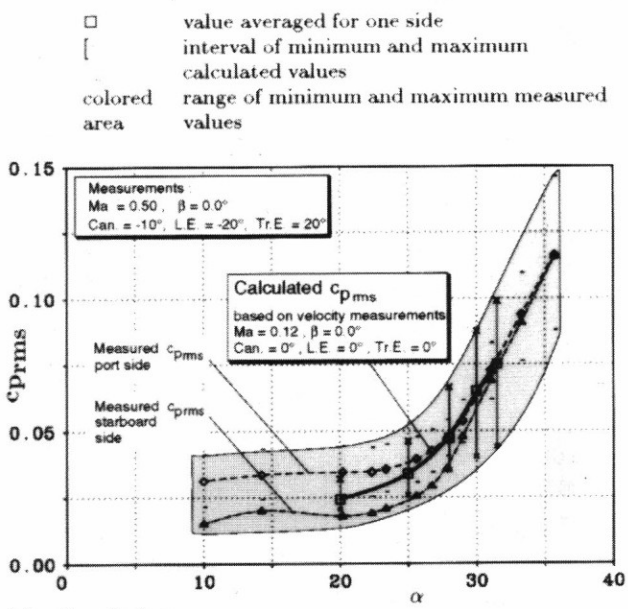

b) $\beta = 0$ deg

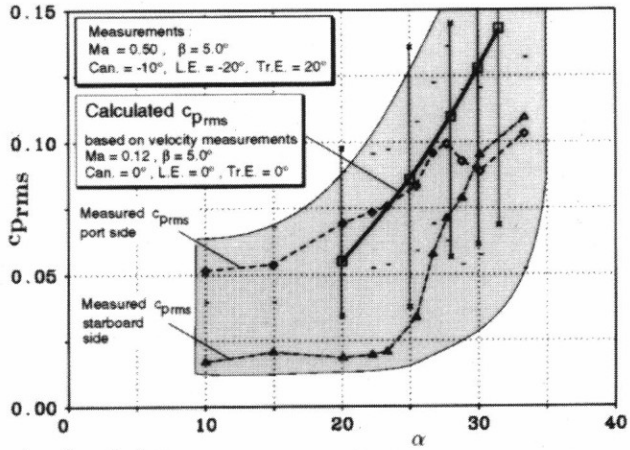

a) $\beta = 5$ deg

Fig. 12 Comparison of calculated with direct measured unsteady fin surface pressure as a function of angle of attack at $\beta = 0$, and 5 deg.

more to the measured values of the leeward (port) side (Fig. 12b). The calculations are based on flowfield measurements performed with the fin section removed where mainly the starboard vortex systems dominate the fin flow without any surface interference. For the fin-on case it seems that interference effects result in increased pressure fluctuations on the port (suction) side. At high-α the averaged values of calculated $c_{p_{rms}}$ show higher levels than those gained from the measurements, but they are below the maximum measured values.

Spectral Content of Calculated Buffet Loads

Figure 13 depicts power spectral densities of the fluctuations in surface pressure difference at station A17 ($X = 0.611, Y = 0.831$) for all angles of attack investigated and for $\beta = 0$, and 5 deg. A staggered spectra plot with respect to the span direction at $X = 0.44$ is shown in Fig. 14 for $\alpha = 28$ deg and $\beta = 0$ deg. In all cases the frequency reso-

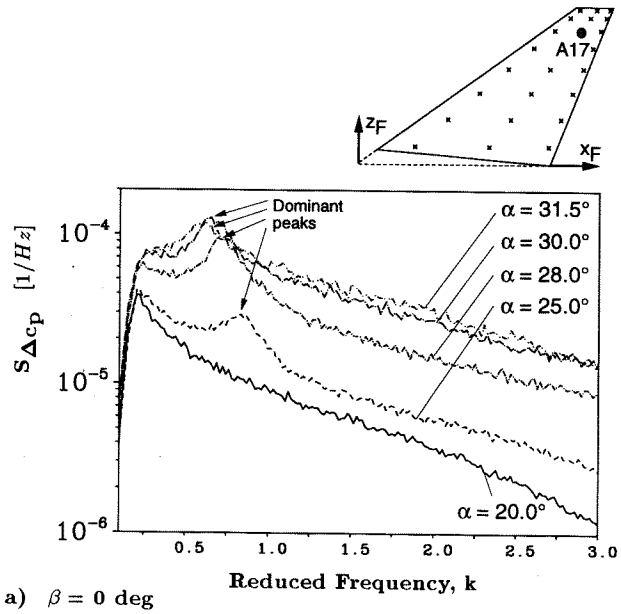

a) $\beta = 0$ deg

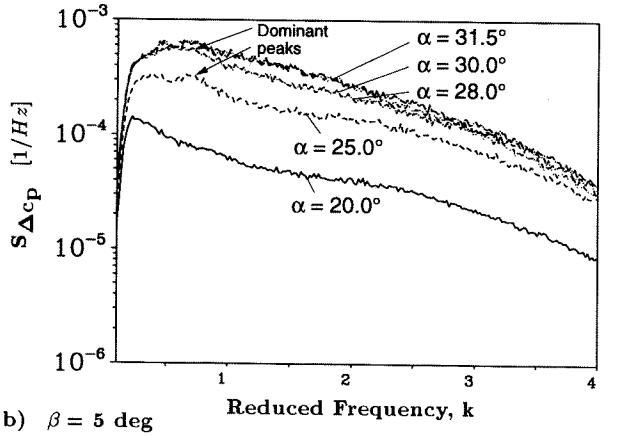

b) $\beta = 5$ deg

Fig. 13 Spectra of unsteady fin surface pressure at station A17 (X = 0.611, Y = 0.831) for various angles of attack at $\beta = 0$, and 5 deg.

lution is 1.95 Hz. At zero sideslip starting at $\alpha = 25$ deg, the spectra exhibit dominant frequencies varying with angle of attack (Fig. 13a). At station A17 the dominant reduced frequency based on the mean areodynamic chord decreases with α in the range of $k = 0.82 - 0.55$. Due to the linear relationship between the oscillations of local incidence and pressure the peaks in pressure spectral density coincide with the frequency peaks detected in the velocity spectra. At a fixed angle of attack the center frequency of the peaks changes slightly with the different stations (collocation points) whereas the content of turbulent kinetic energy differs significantly (Fig. 14). At $\beta = 5$ deg, the spectra becomes widened (Fig. 13b), and turbulent energy increases. The spectra of fluctuating pressure may be used as input for structural analysis as described in Ref. 5.

From the discussion of the pressure field and the related spectra (Figs. 10 and 11, and Figs. 13 and 14) it is seen that an analysis based on the pressure spectra at one location is not representative of the buffet load characteristics. In order to describe the buffet loads accurately signals from a large number of surface positions must be summed. The lifting surface method provides total buffet loads from pressure summation resulting in the power spectral density of the normal force coefficient. For various α and $\beta = 0$ deg, the normal force coefficient spectra are presented in Fig. 15. It is shown that the pressure field contains energy over a moderately wide frequency range, where a peak can be detected at the same value of reduced frequency as in the pressure spectra. The behaviour in normal force fluctuation is quite similar to that observed for F/A-18 twin-fins,[31] however, the energy content is lower nearly one order of magnitude.

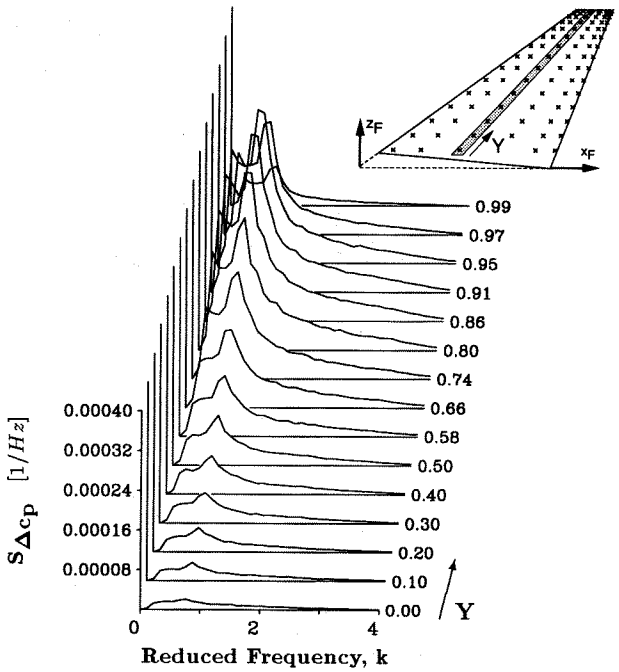

Fig. 14 Spectra of unsteady fin surface pressure at X = 0.44 for various stations in span direction at $\alpha = 28$ deg and $\beta = 0$ deg.

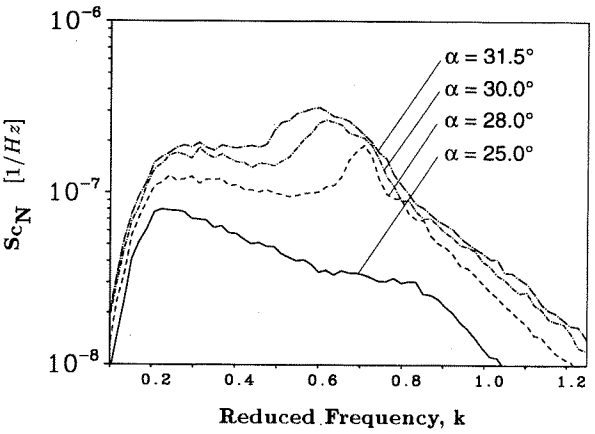

Fig. 15 Spectra of unsteady fin normal force coefficient for various angles of attack at $\beta = 0$ deg.

Dominant Frequency

The variation of dominant reduced frequency with angle of attack, taken from the normal force spectra, is summarized in Fig. 16a. The dominant reduced frequency decreases with α from $k = 0.8$ at $\alpha = 25$ deg to $k = 0.61$ at $\alpha = 31.5$ deg.

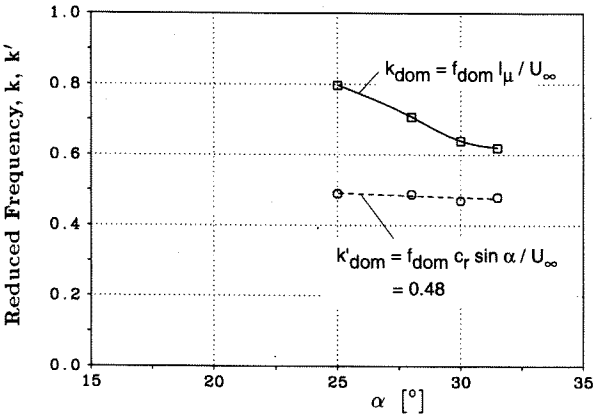

a) **Dominant reduced frequency of buffet load**

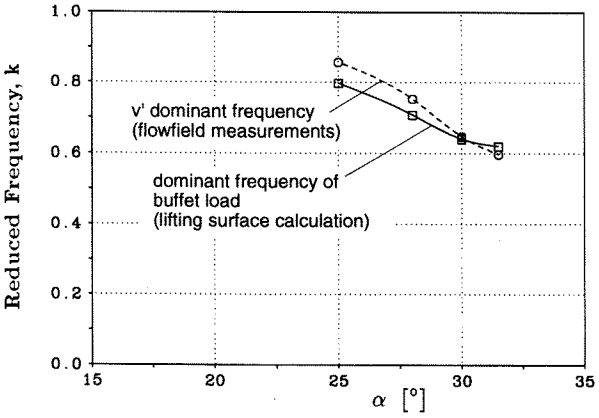

b) **Dominant frequency of flowfield velocity and buffet load**

Fig. 16 Dominant reduced frequency of fin buffet load and flowfield velocity as function of angle of attack at $\beta = 0$ deg.

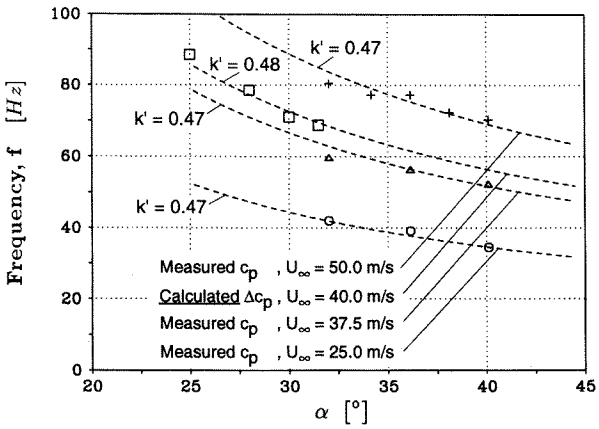

Fig. 17 Comparison of calculated with measured dominant reduced frequency of fin buffet load as function of angle of attack and freestream velocity at $\beta = 0$ deg.

To scale for angle of attack a reduced frequency k' is used based on the projection of the wing root chord normal to the freestream. It is shown that for the different α a value of $k' = 0.48$ matches with the values of k nearly at a straight line. In a plane normal to the freestream the volume of the bursted leading-edge vortex increases with angle of attack, how the frequency of the related quasi-periodic fluctuations decrease. Within a certain incidence range this may be linear. Figure 16b substantiates the similarity in dominant reduced frequency of flowfield and normal force.

An excellent agreement can be detected again when comparing the computed values of k' with the results of Ref. 30 as shown in Fig. 17. For a flexible aircraft, a large structural response could result from the peak in the buffet load spectra which varies with frequency, dynamic pressure and angle of attack. This occurs when the pronounced frequency of the buffet loads coincide approximately with one of the fin natural frequencies. If the dominant frequencies of the buffet loads are well known at an early design stage the structural properties can be easier chosen in a way that tuning of the peak in the buffet load spectra with any of the natural frequencies of the fin is avoided.

Conclusions

A prediction method for fin buffet aerodynamic loads was presented to evaluate unsteady fin surface pressure on a single-finned delta-canard configuration in the range of $\alpha = 20$ to 31.5 deg and at $\beta = 0$, and 5 deg. The method is based on fluctuating flowfield velocity using a modified lifting surface code. The buffeting excitation input was shown to be characterized by increased turbulence intensity with peaked velocity spectra. From the lifting surface method rms values and spectra of fluctuating pressure and normal force were obtained. It was clearly shown that with increasing angle of attack there is an evident increase in unsteady pressure. The pattern of intensity of the pressure fluctuations changes strongly with α depending mainly on the development and interaction of the wing and canard leading-edge vortex systems. Normal force spectra exhibit a distinct narrow-band peak which varies with angle of attack corresponding to that of the velocity spectra. If the peak reduced frequency is based on the projection of the wing root chord normal to freestream a value of 0.48 is obtained which holds approximately for all the incidences regarded. The results were compared to those of direct measurements of fluctuating fin surface pressure. At symmetric freestream an excellent agreement was shown for all α investigated. At sideslip and moderate angle of attack, the calculated fin buffet loads matches with those measured on the leeward side. At high-α averaged fin buffet loads for one side would be overestimated, but are below the level of maximum measured values. It is thought that the prediction method shown herein will be useful for an estimation of buffet load characteristics at an early design stage.

Acknowledgements

The work was supported in part by the Daimler-Benz Aerospace AG (DASA) under the directorat of Dipl.-Ing. W. Kuny. The authors express their appreciation to Dr.-Ing. J. Becker (DASA) for his kind assistance in the research project.

References

[1] Breitsamter, C., and Laschka, B., "Turbulent Flow Structure Associated with Vortex–Induced Fin Buffeting," *Journal of Aircraft*, Vol. 31, No. 4, July-Aug. 1994, pp. 773 – 781.

[2] Breitsamter, C., and Laschka, B., "Turbulent Flowfield Structure Associated with Fin Buffeting Around a Vortex–Dominated Aircraft Configuration at Sideslip," 19th Congress of the International Council of the Aeronautical Sciences, Anaheim, CA, Sept. 1994, ICAS–94–4.3.2, Vol. I., pp. 768 – 784.

[3] Lee, B. H. K., Brown, D., Tang, F. C., and Plosenski, M., "Flowfield in the Vicinity of an F/A–18 Vertical Fin at High Angles of Attack," *Journal of Aircraft*, Vol. 30, No. 1, 1993, pp. 69 – 74.

[4] Del Frate, J. H., and Zuniga, F. A., "In–Flight Flow Field Analysis on the NASA F–18 High Alpha Research Vehicle With Comparisons to Ground Facility Data," AIAA Paper 90-0231, Jan. 1990.

[5] Ashley, H., Rock, S. M., Digumarthi, R. V., Chaney, K. and Eggers, Jr., A. J. "Active Control for Fin Buffet Allevation", WL–TR–93–3099, Flight Dynamics Directorate, Wright Laboratory, Wright Patterson AFB, OH, Jan. 1994.

[6] Bean, E. B., Greenwell, I. D., and Wood N. J., "Vortex Control Technique for the Attenuation of Fin Buffet," *Journal of Aircraft*, Vol. 30, No. 6, 1993, pp. 847 – 853.

[7] Colvin, B. J., Mullans, R. E., Paul, R. J., and Ross, H. N., "F–15 Vertical Tail Vibration Investigations," McDonnell–Douglas Corporation Rep. A6114, McDonnell Aircraft Company, St. Louis, MO, Sept. 15, 1979.

[8] Triplett, W. E., "Pressure Measurements on Twin Vertical Tails in Buffeting Flow," *Journal of Aircraft*, Vol. 20, No. 11, 1983, pp. 920 – 925.

[9] Erickson, G. E., Hall, R. M., Banks, D. W., Del Frate J. H., Schreiner, J. A., Hanley, R. J., and Pulley, C. T., "Experimental Investigation of the F/A–18 Vortex Flows at Subsonic Through Transonic Speeds, Invited Paper," AIAA Paper 89-2222, July 31 - August 2, 1989.

[10] Lee, B. H. K., and Brown, D., "Wind-Tunnel Studies of F/A–18 Tail Buffet," *Journal of Aircraft*, Vol. 29, No. 1, 1992, pp. 146 – 152.

[11] Lee, B. H. K., and Tang, F. C., "Unsteady Pressure and Load Measurements on a F/A–18 Vertical Fin," *Journal of Aircraft*, Vol. 30, No. 5, 1993, pp. 228 – 234.

[12] Martin, C. A., Glaister, M. K., Mac Laren, L. D., Meyn, L. A., and Ross, S., "F/A–18 1/9th Scale Model Tail Buffet Measurements," Aeronautical Research Lab. Flight Mechanics Rept. 188, June 1991.

[13] Shah, G. H., "Wind Tunnel Investigation of Aerodynamic and Tail Buffet Characteristics of Leading–Edge Extension Modifications to the F/A–18," AIAA Atmospheric Flight Mechanics Conf., AIAA Paper 91-2889, Aug. 1991, pp. 395 – 412.

[14] Meyn, L.A., Lanser, W. R., and James, K. D., "Full–Scale High Angle–of–Attack Tests of an F/A–18," AIAA 10th Applied Aerodynamics Conf., AIAA Paper 92-2676, Palo Alto, CA, June 22-24, 1992.

[15] Lee, B. H. K., Brown, D., Zgela. M., and Poirel, D., "Wind Tunnel Investigations and Flight Tests of Tail Buffet on the CF–18 Aircraft," AGARD–CP–483, Aircraft Dynamic Loads due to Flow Separation, Sorrento, Italy, April 1990, pp. 1-1 – 1-26.

[16] Hebbar, S. K., Platzer, M. F. and Liu, D.-M., "Effect of Canard Oscillations on the Vortical Flowfield of a X–31A–Like Fighter Model in Dynamic Motion," AIAA–93–3427–CP, AIAA Applied Aerodynamics Conf., Monterey, CA, Aug. 1993, Part 1, pp. 241 – 250.

[17] Mabey, D. G., and Pyne C. R., "Fin Buffeting at High Angles of Incidence on a Model of Slender Wing Aircraft," International Forum on Aeroelasticity and Structural Dynamics, Aachen, Germany, June 1991, Paper 91-129, 1991, pp. 552 – 561.

[18] Breitsamter, C., "Experimentelle Untersuchung der instationären Feldgrößen und Oberflächendrücke bei wirbeldominierter abgelöster Strömung," Deutscher Luft- und Raumfahrtkongreß, DGLR–Jahrestagung, DGLR–JT95–062, Bonn–Bad Godesberg, Sept. 26-29, 1995, Vol. I, pp. 163 – 175.

[19] Kwon, O. J., and Sankar, L. N., "Viscous Flow Simulation of Fighter Aircraft," AIAA 29th Aerospace Sciences Meeting, AIAA Paper 91-0278, Reno, NV, Jan. 7-10, 1991.

[20] Schiff, L. B., Cummings, R. L., Sorenson, R. L., and Rizk, Y. M., "Numerical Simulation of High–Incidence Flow over the Isolated F–18 Fuselage Forebody," *Journal of Aircraft*, Vol. 28, No. 10, Oct. 1991, pp. 609 – 617.

[21] Rizk, Y. M., and Gee, K., "Numerical Prediction of the Unsteady Flowfield Around the F–18 Aircraft at Large Incidence," AIAA 29th Aerospace Sciences Meeting, AIAA Paper 91-0020, Reno, Nv, Jan. 7-10, 1991.

[22] Edwards, J. W., "Assessment of Computational Prediction of Tail Buffeting," NASA TM 101613, Jan. 1990.

[23] Zimmermann, N. H., Ferman, M. A., Yurkovich, R. N., and Gerstenkorn, G., "Prediction of Tail Buffet Loads for Design Applications," AIAA Paper 89-1378, 1989.

[24] Lee, B. H. K., "A Method for Predicting Wing Response to Buffet Loads," *Journal of Aircraft*, Vol. 21, No. 1, 1984, pp. 85-87.

[25] Breitsamter, C., and Laschka B., "Velocity Measurements with Hot–Wires in a Vortex–Dominated Flowfield," AGARD–CP–535, Wall Interference, Support Interference and Flow Field Measurements, Brussels, Belgium, Oct. 1993, pp. 11-1 – 11-13.

[26] Breitsamter, C., "Messungen und Analyse der zeitabhängigen Geschwindigkeiten im wirbeldominierten Strömungsfeld eines Hochleistungsflugzeuges, Teil 1," FLM–91/22, Lehrstuhl für Fluidmechanik, Technische Universität München, München 1991.

[27] Breitsamter, C., "Ein Beitrag zum Phänomen des Seitenleitwerks–Buffeting an wirbeldominierten Flugzeugkonfigurationen," FLM–94/4, Lehrstuhl für Fluidmechanik, Technische Universität München, München, 1994.

[28] Laschka, B., "Zur Theorie der harmonisch schwingenden tragenden Fläche bei Unterschallanströmung," *Zeitschrift für Flugwissenschaften*, 11. Jahrgang, Heft 7, Juli 1963, pp. 261 – 292.

[29] Watkins, C. E., Runyan, H. L., and Woolston, D. S., "On the Kernel function of the Integral Equation Relating the Lift and Downwash Distributions of Oscillating Finite Wings in Subsonic Flow," NACA TR 1234, 1955.

[30] Breitsamter, C., "Berechnung der instationären Drücke am Seitenleitwerk einer Delta–Canard–Konfiguration auf der Basis experimentell ermittelter Geschwindigkeiten," FLM–95/14, Lehrstuhl für Fluidmechanik, Technische Universität München, München, 1995.

[31] Lee, B. H. K., and Tang, F. C., "Characteristics of the Surface Pressures on a F/A–18 Vertical Fin Due to Buffet," *Journal of Aircraft*, Vol. 31, No. 1, 1994, pp. 228 – 234.

[32] Bendat, J. S., and Piersol, A. G., "Random Data: Analysis and Measurement Procedures," J. Wiley & Sons, Inc. Ney York, 1971.